Journal of Geophysical Research: Oceans

RESEARCH ARTICLE
10.1029/2018JC013859

Key Points:
- Sea surface wave spectra are obtained, with expanded high wave number bandwidth and improved sensitivity to wind forcing response
- Emergence of a gravity-capillary spectral peak is found to occur near the critical wind forcing magnitude u_*~0.045 m/s
- Wind sea-coherent microbreaking events are shown to modulate centimeter-scale surface roughness

Supporting Information:
- Supporting Information S1
- Movie S1
- Movie S2
- Movie S3
- Movie S4

Correspondence to:
N. J. M. Laxague,
laxague@ldeo.columbia.edu

Citation:
Laxague, N. J. M., Zappa, C. J., LeBel, D. A., & Banner, M. L. (2018). Spectral characteristics of gravity-capillary waves, with connections to wave growth and microbreaking. *Journal of Geophysical Research: Oceans*, *123*, 4576–4592. https://doi.org/10.1029/2018JC013859

Received 30 JAN 2018
Accepted 16 MAY 2018
Accepted article online 12 JUN 2018
Published online 5 JUL 2018
Corrected 30 JUL 2018

This article was corrected on 30 JUL 2018. See the end of the full text for details.

Spectral Characteristics of Gravity-Capillary Waves, With Connections to Wave Growth and Microbreaking

Nathan J. M. Laxague[1], **Christopher J. Zappa**[1], **Deborah A. LeBel**[1], **and Michael L. Banner**[1,2]

[1]Ocean and Climate Physics Division, Lamont-Doherty Earth Observatory, Columbia University, Palisades, NY, USA, [2]School of Mathematics and Statistics, University of New South Wales-Sydney, Sydney, Australia

Abstract In order to improve our understanding of physical air-sea interaction, it is essential to better describe the short-scale ocean wave response to wind forcing. This is particularly true for waves which are small enough to evade observation by traditional buoy and point-based gauge measurements but large enough to appreciably alter the transfer of momentum between atmosphere and ocean. Such waves are restored to equilibrium both by the Earth's gravity and air-sea surface tension, hence the classification as "gravity-capillary." Radar remote sensing techniques depend greatly upon these waves in order to extract useful physical parameters from afar. Despite this importance, field observations of gravity-capillary wave characteristics are uncommon and results vary from study to study. Furthermore, leading-edge model wave number spectra generally do not match each other in shape or important spectral parameters. Here we present an extended analysis of short wave data collected via a polarimetric camera aboard Research Platform Floating Instrument Platform in the Santa Barbara Channel. Our wave number saturation spectra show the emergence of a peak in the gravity-capillary subrange at low wind forcing magnitude (u_*~0.045 m/s), consistent with critical wave growth in air side stability theory and previously only observed in the laboratory. Finally, the effects of microbreaking on wave spectral characteristics are discussed.

Plain Language Summary High-resolution, short-scale wave slope data are analyzed. The connection between wind forcing and the relative energy levels of different scales of short waves is explored. A sharp transition in wave energy distribution is observed at low wind forcing, corresponding to the growth of centimeter-scale waves. A case study is presented in which short scale wave breaking events are explored.

1. Introduction

Ocean surface waves play a crucial role in physical air-sea interaction, with the majority of air-sea momentum flux being mediated through them (Grare, Peirson, et al., 2013). Waves with length scales of centimeters and smaller possess substantial local curvature, leading to air-water surface tension becoming an important force for restoring the interface to equilibrium (Maxwell, 1890). In this subrange, the physical characteristics of the sea state—among them the broadly termed "surface roughness"—profoundly affect radiative transfer (Jin et al., 2006; Wei et al., 2014; You et al., 2011) and have been hypothesized to dominate momentum flux for low to moderate wind forcing (Donelan & Plant, 2009; Kudryavtsev & Makin, 2002). Furthermore, centimeter-scale sea surface roughness elements are the principal scatterers of microwave electromagnetic radiation (Plant, 2002), making the waves of great interest to the radar remote sensing community. The complex nature of a multicomponent, multidirectional sea state necessitates the distillation of easily digestible wave parameters from the full spatiotemporal record. Past studies have performed such decompositions of short wavefields with the help of statistical tools (Caulliez & Guérin, 2012; Cox & Munk, 1954; Mironov et al., 2012) and Fourier analysis (Hara et al., 1998; Hwang et al., 1996; Laxague et al., 2015; Yurovskaya et al., 2013; Zappa et al., 2012). However, obtaining the field data needed to fuel these analyses is a difficult proposition. This is primarily due to the fact that the physical characteristics of centimeter-scale ocean waves cannot be measured by such traditional devices as buoys, capacitance gauges, or lidar. The fundamental issue involves the disturbance of fine-scale fluid mechanical features by a bulky instrument; a secondary problem arises from the waves' strong sensitivity to advection by long wave orbital motions and background current. The latter concern manifests by way of a Doppler shift which is challenging to decouple from the intrinsic properties of the waves themselves. As a result, the most palatable method by far for recovering centimeter-scale wave parameters involves the use of advanced imaging devices. Stereoscopic camera systems allow for the resolution of short gravity waves (Benetazzo, 2006); improved and expanded algorithms may extend this resolution to the gravity-capillary subrange (Kosnik & Dulov, 2011; Yurovskaya et al., 2013). PSS (Zappa et al., 2008) is especially well-suited toward capturing small-scale wave characteristics. It enables the user to obtain spatial arrays of directional wave slope from a single camera enclosure, with resolution constrained only by that of the camera itself; with modern cameras, standard lenses, and shipboard mounting, this resolution is typically well into the regime of pure capillary waves (wavelength of order 1 mm). The present work describes the analysis of a data set of short wave slope fields which were obtained from Research Platform FLIP (Floating Instrument Platform) in the Santa Barbara Channel, expanding on some preliminary results offered in Zappa et al. (2012). It is a study of spectral shape over the wave number subrange for which gravity and surface tension are both relevant restoring forces to equilibrium, in the vein of Laxague et al. (2015). Here we expand deeper into the nature of specific spectral features and the associated forcing mechanisms. For example, the relationship between wind forcing and the transition in the dominant gravity-capillary wave scale is explored. Additionally, connections are drawn between the shape of the spectral tail and the presence of nonair-entraining microbreaking waves.

What follows is an explanation of the observational methods (section 2), a description of the results relevant to this work (section 3), a discussion of their implications for physical air-sea interaction (section 4), and concluding remarks (section 5).

2. Materials and Methods

Data were collected aboard Research Platform FLIP in the Santa Barbara Channel (Figure 1) as part of the Office of Naval Research Radiance of the Dynamic Ocean (RaDyO) campaign in Fall 2008. A thorough description of that campaign's overriding objectives, design, and broad results may be found in Zappa et al. (2012). The motivations of the present study guided our focus toward two segments of the overall data set: the air-sea momentum flux and the spatiotemporal behavior of short-scale ocean waves. For the former, the three-dimensional wind velocity vector was sampled at 20 Hz via a Campbell Scientific CSAT sonic anemometer affixed to the end of FLIP's boom (Figure 1c). At the same location, a downward-looking Riegl model LD90-3-3100VHS lidar was mounted in order to retrieve water surface elevation, thereby resolving the longer ocean surface gravity waves. Its footprint on the water surface was on the order of 10 cm in diameter. A spectrogram produced from the lidar water surface elevation time series is shown in Figure 2. It is resolved to $f = 1$ Hz in the frequency domain, corresponding approximately to the scale at which the instrument reaches its noise floor (as shown in Figure 7 of Lenain & Melville, 2017). FLIP's motion was minimal: Root-mean-square (RMS) vertical platform velocities (as computed from the onboard six degree of freedom inertial motion unit) were found to be less than 1% of the RMS vertical wind velocities. Once the wind vector time series had been transformed into along and cross-stream coordinates, wind stress (and the friction velocity u_*) was computed using the eddy covariance technique (e.g., Edson et al., 2013). A substantial portion of the present study involves the comparison of our observations to those described in other published works. For many of these other studies, u_* is not reported; as a result, an empirical formula was used to estimate the bulk friction velocity from the reported 10-m neutral wind speed. The model spectrum of Hwang and Fois (2015) uses the Wu (1982) parameterization. For the sake of consistency, we followed suit.

The other component of the data set—the short-scale ocean wave physical properties—was obtained via polarimetric camera and the polarimetric slope sensing (PSS) method of Zappa et al. (2008). A total of 62 camera runs were executed, each approximately 20 min long. After initial quality control, 16 were deemed appropriate for use in extracting meaningful physical parameters. This seemingly austere level of rejection is largely due to the contamination of images by Sun glitter, an issue that is difficult to avoid on the fixed-orientation FLIP. Sun glitter prevents the determination of sea surface slopes by saturating the image at all linear polarizations, thereby rendering large patches of the imaged surface unusable in the computation. In order to bypass this issue, the only camera runs kept for analysis were those acquired during overcast days or during periods of no visible Sun glint. The camera used for this experiment was the custom-built device described in Zappa et al. (2012), designed to minimize sensor integration time (~1 ms) and therefore the smothering effect of motion blur on the shortest ocean waves. Fixed-pattern noise was mitigated by way of a nonuniformity correction. The PSS makes use of light intensity data fields (here visible imagery) corresponding to 0, 45, and 90° linear polarizations. The output of this method is—for each image—a slope vector field (s_x and s_y, Figure 3) at the camera spatial resolution. Slope fields were rectified to the sea surface (Laxague, 2016)

10.1029/2018JC013859

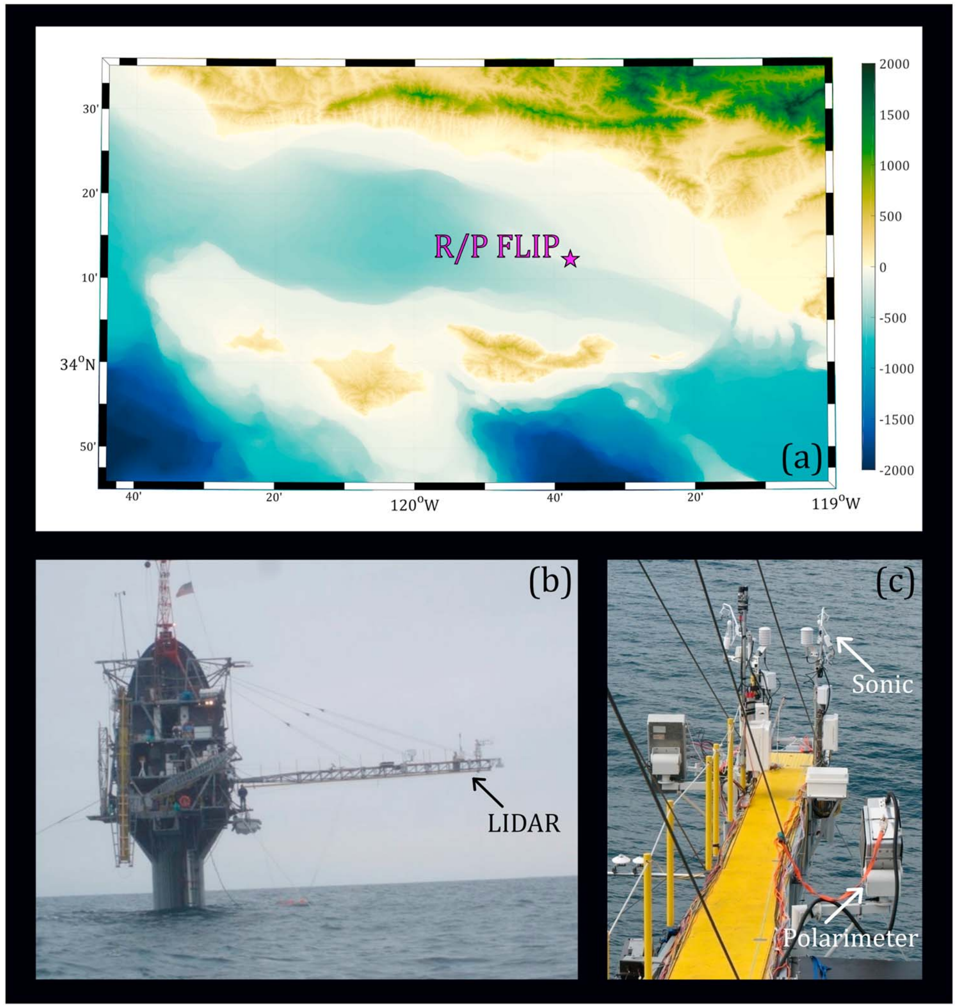

Figure 1. (a) Map of Santa Barbara Channel, with Research Platform Floating Instrument Platform (FLIP) location indicated by the magenta five-pointed star. The color bar indicates displacement of solid Earth from mean sea level. (b) Side view of the fully deployed FLIP. (c) Close-up of the FLIP boom. Bathymetric data used to color (a) were obtained from Divins and Metzger. The arrows in (b) and (c) indicate the position of the Riegl lidar, sonic anemometer, and the polarimetric camera.

accounting for the camera's 37° incidence angle to produce square arrays of isotropic spatial scale of ~1.37 mm/pixel. In some of the supplementary videos contained within the Supporting Information, the water surface elevation fields are shown. These were computed by integrating the observed slope fields using the algorithm of Harker and O'Leary (2008).

In order to prepare these slope field arrays for their use in Fourier analysis, they were subjected to Tukey (tapered cosine) windows (Harris, 1978), here of taper width 0.2. This step was performed in order to reduce the contamination of the low wave number portion of each spectrum by frame edge-induced artifacts. Smoothing filters—either of the median or convolution variety—were not used on slope fields in this study. The Appendix offers an explanation for this choice. After windowing, the arrays were stacked in blocks of 10 s worth of data and transformed via fast Fourier transform ($F[\ldots]$) in order to compute the directional wave number-frequency slope spectra $S(k_x, k_y, \omega)$. These were averaged in time to produce a robust description of the short ocean wave state (Laxague, Haus, et al., 2017).

$$g_x = \mathscr{F}[s_x(x,y,t)] \quad g_y = \mathscr{F}\left[s_y(x,y,t)\right]$$

$$S(k_x, k_y, \omega) = \frac{|g_x|^2 + \left|g_y\right|^2}{N k_{\max}^2 \omega_s}$$

10.1029/2018JC013859

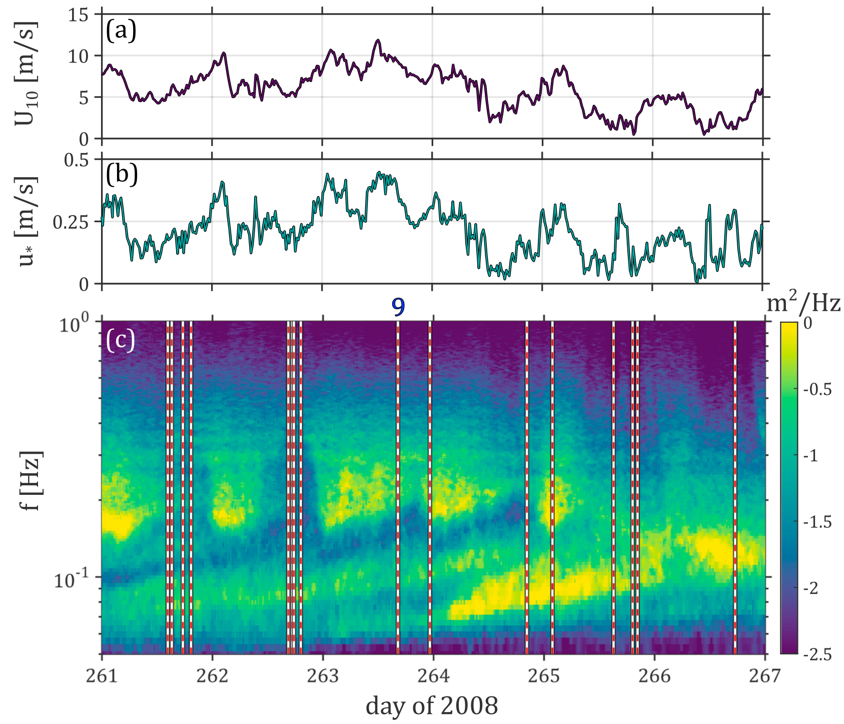

Figure 2. Time series of selected environmental conditions: (a) Ten-meter neutral wind speed and (b) friction velocity u_* c wave height frequency spectrogram. The color bar indicates spectral energy density in m^2/Hz. The dashed red and white lines mark the instances of polarimetric camera acquisition. Run 9 is labeled with a blue number at the top of the figure.

Here N is the number of data points, $k_{\max}$ is the resolution wave number, ~4,581 rad/m, and ω_s is the camera's sampling frequency in radians per second. The wave number-frequency behavior of these spectra (i.e., dispersive properties of the waves) is outside the scope of the present study. In order to produce the fully directional wave number spectra, all wave number-frequency spectra were integrated over positive frequencies, eliminating the 180° ambiguity which would be present in the spectrum computed from a single frame. Due to the fact that the camera's Nyquist frequency was 30 Hz, however, not all waves seen in the slope fields were resolved temporally. To complicate matters further, the great majority of the observed gravity-capillary waves were bound to longer waves (Laxague, Haus, et al., 2017; Plant, Dahl, et al., 1999; Plant, Keller, et al., 1999), greatly increasing their observed celerities. This prevented our resolving the temporal development of waves at gravity-capillary scales (order of $k > 100$ rad/m) and smaller; in short, the 180° ambiguity persists for the waves which are the focus of the study. Additionally, despite the fact that FLIP is quite rigid and stationary as a platform compared to research vessels, its slight rotations (typically slower than 1 deg/s) will still affect the remote determination of wave propagation characteristics, especially at small scales. For this reason, the full wave number-frequency spectrum was used only to eliminate the 180° ambiguity of the dominant short gravity waves (e.g., the example two-dimensional spectrum shown in Figure 3). Future studies which seek to describe the spatiotemporal properties of gravity-capillary waves will need to continue to address these issues. Analysis of the present data focuses on the omnidirectional properties of the short-scale waves, with fully directional characteristics described only qualitatively in Figure 3 and in the Supporting Information. Movie S1 in the supporting information shows the directional wave spectra for all cases and indicates the wave number cutoff for unambiguous directional analysis.

The wave number spectra were clipped at k = 1,600 rad/m to eliminate the contamination of the remaining fixed-pattern noise. Note that the water surface elevation spectrum $\Psi(k_x, k_y) = k^{-2}S(k_x, k_y)$ and the dimensionless saturation spectrum $B(k_x, k_y) = k^2S(k_x, k_y)$ (Phillips, 1984). The latter is often used when one wishes to characterize high wave number spectral shape (Jähne & Riemer, 1990; Yurovskaya et al., 2013). A typical directional wave number saturation spectrum is shown in the lower panels of Figure 3 with respect to both Cartesian (c) and polar (d) variables. Note the directional ambiguity which appears for $k > 172$ rad/m—the

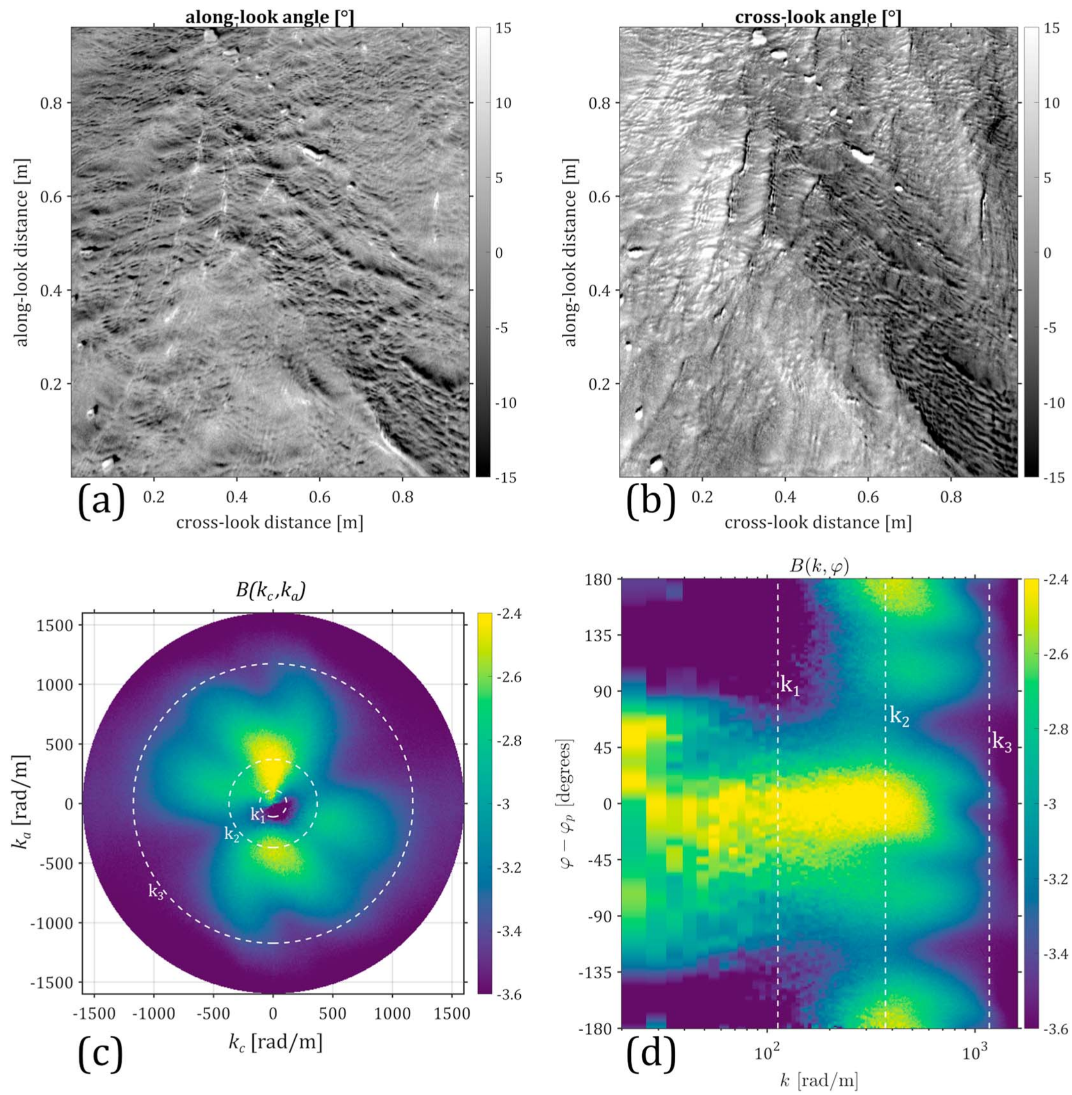

Figure 3. (a) Along-look and (b) cross-look water surface angle maps generated using the polarimetric slope sensing. Note that the gray scale intensity corresponds to the water surface angle in degrees. (c) Two-dimensional Cartesian (cross, along) wave number saturation spectrum, generated from a 10-s long data stream. (d) Same spectrum, represented in terms of wave number k and azimuth angle φ, referenced to wind velocity direction. The dashed lines k_1, k_2, and k_3 correspond to 112.7, 371, and 1,173 rad/m, respectively, the boundaries of GC1 and GC2. The properties of the spectrum represented in (c) and (d) are stationary over the course of the full 20-min acquisition.

region in which spatiotemporal wave evolution is not captured by the camera system. The omnidirectional wave number saturation spectrum may be obtained by integrating the directional spectrum azimuthally. We first convert from Cartesian to polar coordinates (notice the Jacobian k in the integrand) and integrate with respect to azimuth angle φ:

$$B(k) = \int_{-\pi}^{\pi} kB(k,\varphi)\mathrm{d}\varphi$$

Although the present study focuses on the characteristics of wave number spectra, it is often useful to compute the corresponding frequency spectra for comparison with other results. The proper way to perform this conversion is described in Plant (2009). An example frequency spectrum computed in this way is shown alongside a frequency spectrum computed from the lidar data in Figure S1 in the supporting information. Given that the zeroth moment of the omnidirectional wave number slope spectrum is the slope variance, the quantity is commonly estimated via integral. By changing the limits of integration, we change the subrange of scales over which slope variance is computed—essentially, a band-pass filter for the ocean surface roughness. Using $S(k) = k^{-1}B(k)$:

$$\sigma_{ij}^2 = \int_{k_i}^{k_j} k^{-1}B(k)dk$$

This technique has been applied either to constrain the wave number subrange for comparison to past studies (Yurovskaya et al., 2013) or to partition wave slope variance by scale in order to answer questions about surface roughness sensitivity to wind forcing (Frew et al., 2004; Laxague et al., 2015; Laxague, Curcic, et al., 2017). For the latter topic, it becomes relevant to mention the linear dispersion relation for gravity-capillary waves in deep water, given below:

$$\omega^2 = gk + \frac{\gamma}{\rho}k^3$$

Here ω is the wave radian frequency in rad/s, g is the acceleration due to gravity (taken as 9.81 m/s^2), γ is the air-water interfacial tension (taken as 0.072 N/m), and ρ is the density of seawater (taken as 1,030 kg/m^3). By using this relation with the parameters given as listed, we may partition waves by scale with regard to dominant restoring force. For 112.7 rad/m $< k <$ 1,173 rad/m, the two right-hand side terms of the dispersion relation are of the same order of magnitude, with k = 371 rad/m marking the point at which they are approximately equivalent. These three values (112.7, 371, and 1,173 rad/m) demarcate two wave number regimes which are of equal width in logarithmic space, named "gravity-capillary #1" (or "GC1") and "gravity-capillary #2" (or "GC2"; Laxague, Curcic, et al., 2017) which will be highlighted in the coming analysis.

3. Results

A sample directional wave spectrum is shown in Figure 3. Because the spectrum was produced from only a 10-s long data stream, transient features are not averaged over, and one can make a qualitative connection between wave components shown in Figures 3a and 3b and the spectral lobes seen in Figures 3c and 3d. This is especially apparent in Movie S2. The form of the spectrum shown in Figure 3d brings to mind the directional wave number spectra presented in Lenain and Melville (2017), especially their Figure 3. These were generated from the water surface elevation fields obtained via airborne scanning lidar and span 0.01 $< k <$ 10 rad/m in wave number space. A prominent feature of these spectra, their ±90° weakly lobed spreading, appears to some extent in the lower wave number range of our Figure 3d. However, the RaDyO spectra do not resolve well the short gravity waves which form the link between Lenain and Melville (2017) and the present work, so this topic will have to be explored further in a future study.

Three examples of wave slope fields and the corresponding 2-D probability density functions (PDFs), computed from 2-min data streams, are given in Figure 4. These are shown in order to provide the reader with a tangible representation of sea surface roughness at varying levels of wind forcing. The volume bounded by the PDF surfaces and the x-y plane have all been normalized to unity. The "normalized" PDFs are so named because the along-wind and cross-wind slopes have been divided by the corresponding directional wave slope standard deviations:

$$\widehat{s}_a = \frac{s_a}{\sigma_a} \qquad \widehat{s}_c = \frac{s_c}{\sigma_c}$$

where again, subscripts a and c represent "along-wind" and "cross-wind." This is a measure designed to emphasize the shape of the PDFs at different levels of wind forcing and follows the convention described in Munk (2009). The lowest and highest-wind forcing cases (#15 and #9, respectively, on the left and right of the figure) contain the canonical pear-shaped PDFs seen in the high wind forcing example of Figure 5 in Munk (2009). For these cases, the highest wave slopes are likeliest in the along-wind direction and least likely in the upwind direction, with symmetric cross-wind propagation. The middle case (#1) is skewed in the along-wind direction but indicates that the highest slopes are in fact likeliest in the cross-wind direction. Movie S3 indicates that the short wave slope PDF characteristics are strongly impacted by longer waves. In

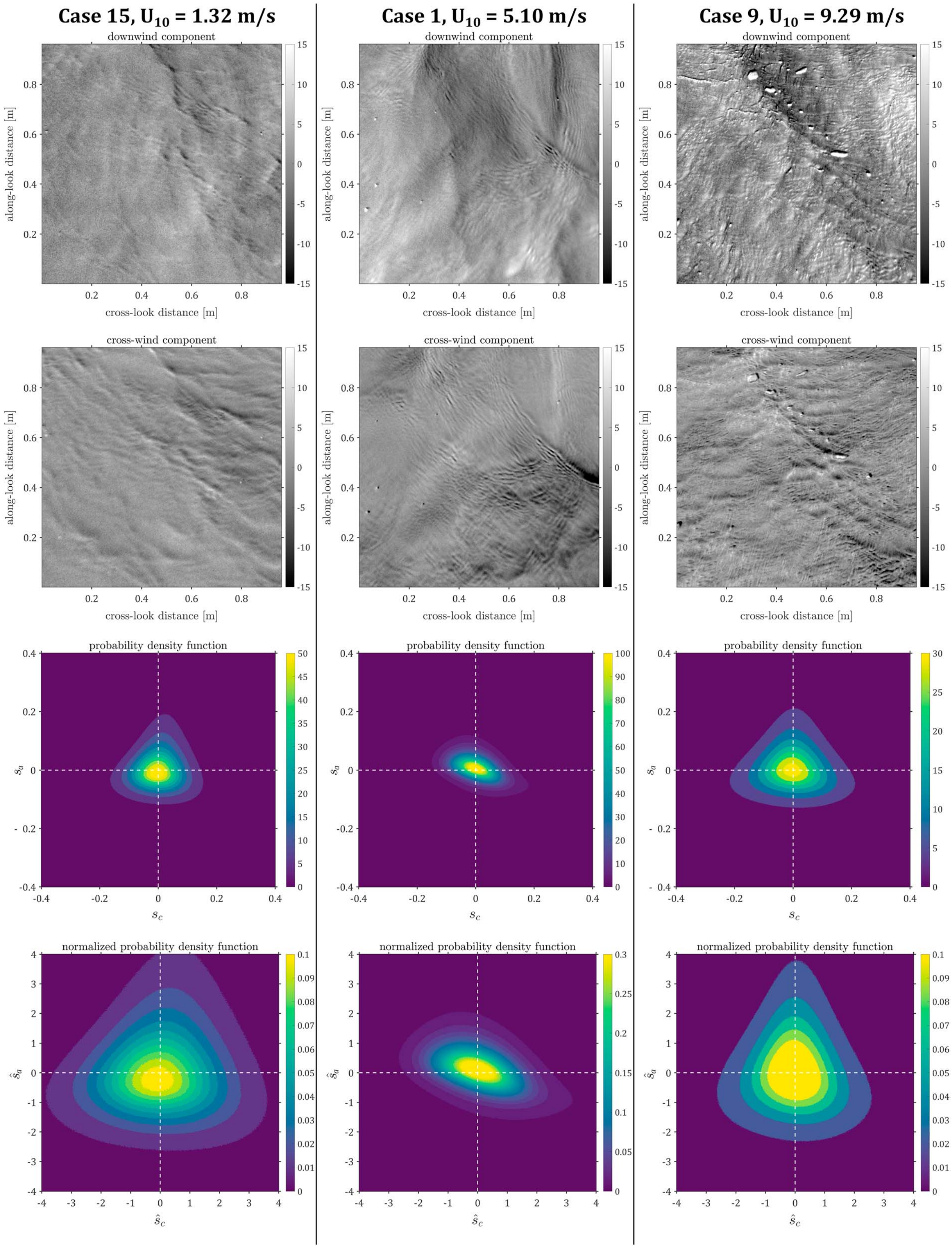

Figure 4. Along-wind and cross-wind slope components with their corresponding 2-D slope probability density functions (PDFs); each column is one of three selected (low, medium, and high) wind forcing cases. The "normalized" PDFs are described in the first paragraph of section 3.

10.1029/2018JC013859

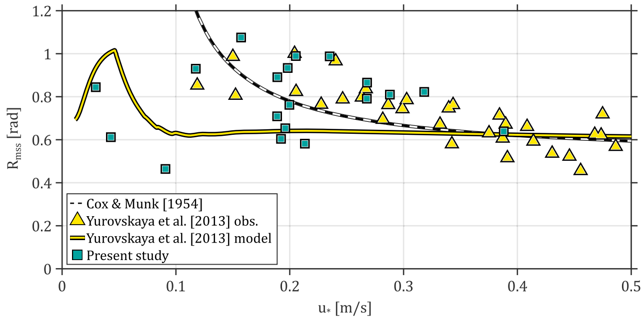

Figure 5. Ratio of cross-wind to along-wind mean square slope, shown alongside the empirical fit given in Cox and Munk (1954) and both the observations and model of Yurovskaya et al. (2013), following the "short wave" (20 rad/m < k < 1,000 rad/m) convention of that paper.

order to properly investigate the disparate roles of wind forcing and long wave dynamics in the shape of these PDFs, additional data sets like the one collected during RaDyO are needed.

The ratio of cross-wind mean square slope to along-wind mean square slope (here $R_{mss} = \sigma_c^2/\sigma_a^2$) is a commonly invoked measure of the directional spreading of short-scale waves. Figure 5 shows a comparison of R_{mss} computed from the spectra of this study (hereafter RaDyO) to those computed from observations and the model in Yurovskaya et al. (2013). There is general qualitative agreement in this parameter over their region of overlap in wind forcing. The Yurovskaya et al. (2013) model does not reflect the higher (0.8–1.0) value observed in the intermediate ($0.15 < u_* < 0.3$ m/s) wind forcing subrange. At lower wind forcing magnitudes, observations depart from Cox and Munk (1954) and follow the model prediction of Yurovskaya et al. (2013), a modification of the Kudryavtsev et al. (1999) model.

Omnidirectional wave number saturation spectra are shown in Figure 6, with RaDyO spectra shown in all panels but colored only in (a); these are given alongside lines of $k^{1/2}$ and k^0 representing the canonical equilibrium and saturation regime slopes, with k^{-1} standing in as the approximate tail slope of the RaDyO spectra. Of the models, Hwang and Fois (2015) agree best with RaDyO spectra in both tail slope and range of spectral density in the GC2 subrange. The pronounced short wave spectral peak seen in many of the RaDyO spectra is also represented in the models of Elfouhaily et al. (1997) and Yurovskaya et al. (2013), with the gravity-

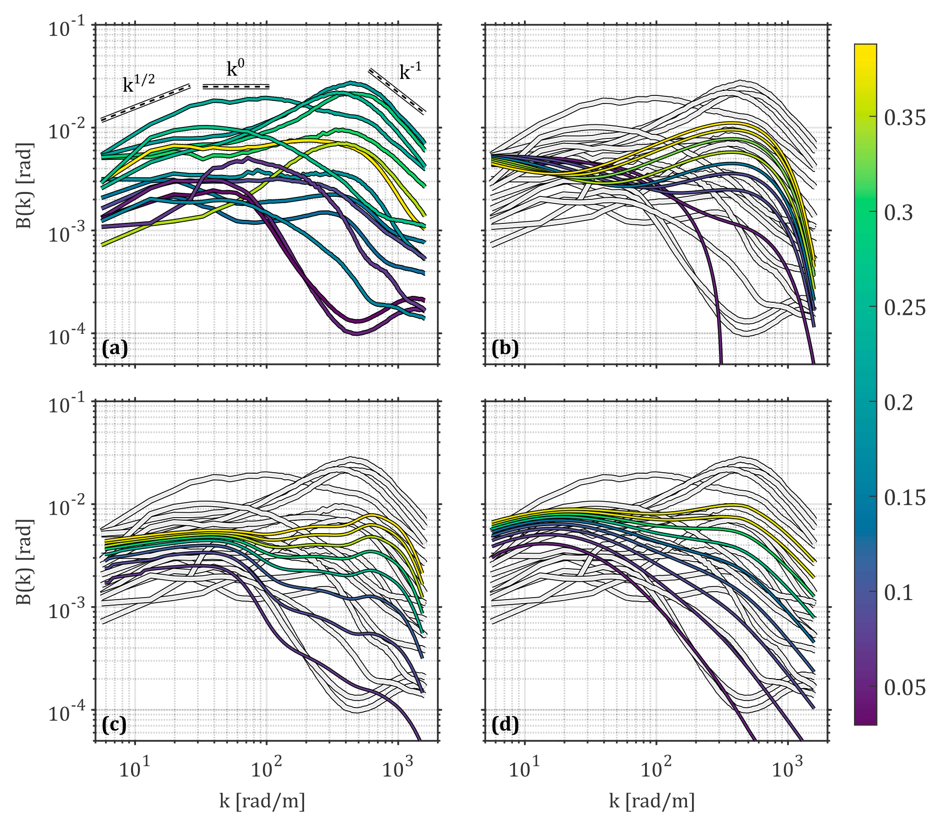

Figure 6. (a) Omnidirectional wave number saturation spectra $B(k)$ produced from observations described in this work. These results are also copied as whitened background lines in each of the following panels in this figure and in Figure 7. The dashed lines indicate spectral slopes (log-log) of $k^{1/2}$, k^0, and k^{-1}. (b) The model spectrum of Elfouhaily et al. (1997). (c) The model spectrum of Yurovskaya et al. (2013). (d) The model spectrum of Hwang and Fois (2015). The color bar indicates wind friction velocity u_* in m/s.

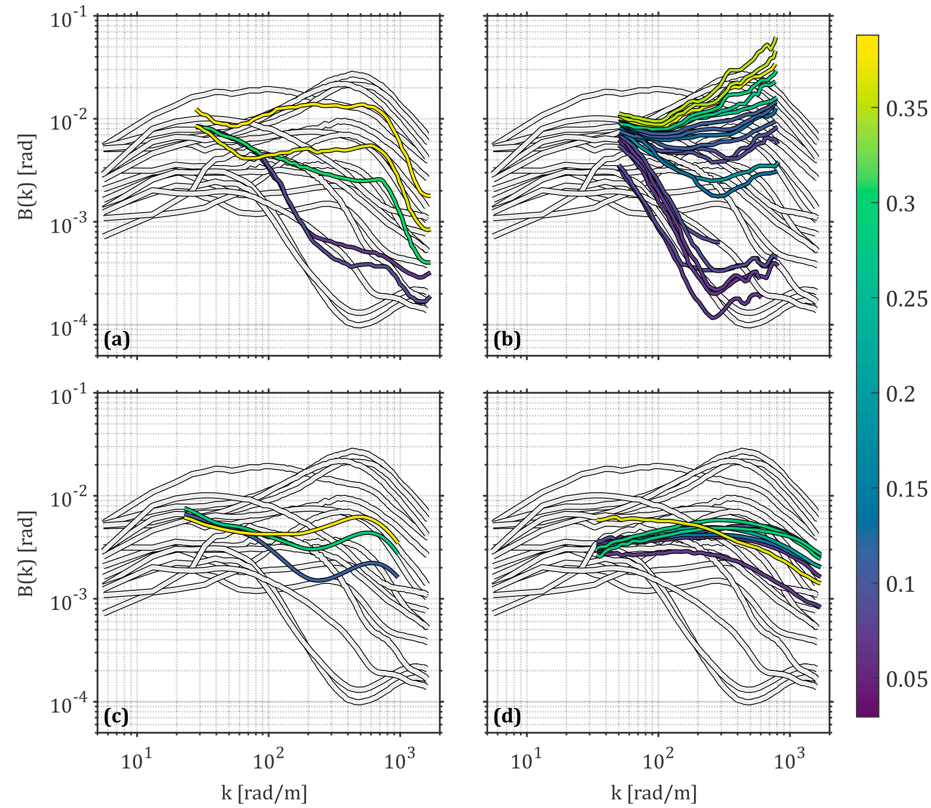

Figure 7. (a) Omnidirectional wave number saturation spectra $B(k)$ produced from the observations of Jähne and Riemer (1990), (b) those produced from the observations of Hara et al. (1998), (c) those produced from the observations of Yurovskaya et al. (2013), and (d) those produced from the observations of Laxague et al. (2015). The color bar indicates wind friction velocity u_* in m/s.

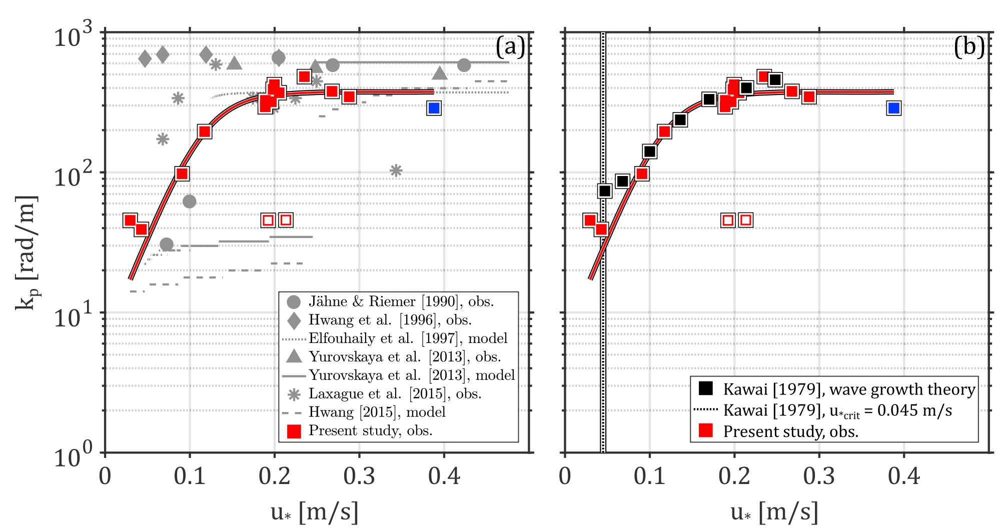

Figure 8. (a) Wave number position, k_p, the peak of the omnidirectional saturation spectrum. (b) The RaDyO values of k_p, alongside those of Kawai (1979a); the critical wind friction velocity $u_{*\text{crit}}$ = 0.045 m/s is marked by a black dotted line. The two open squares correspond to run numbers 12 and 16. Run 9 has the strongest wind forcing and is indicated by a blue square. The curve of best fit is the logistic function $Q(u_*) = \frac{Q_\infty}{1+e^{-b(u_*-u_{\text{half}})}}$, where Q_∞~375.13 rad/m, b~35.23 m^{-1}s, and u_{half}~0.116 m/s.

Table 1
Wind and Gravity Wave Conditions From Times of Observation Gray Shaded Rows Indicate Cases Which Are Swell-Dominated

Run number	U_{10} [m/s]	u_* [m/s]	Wind dir. [deg.]	T_p [s]	H_s [m]	$k_pH_s/2$ [rad]	C_p [m/s]	C_p/u_*
1	5.10	0.189	256.4	4.32	0.68	0.073	6.74	35.67
2	6.19	0.189	262.4	4.07	0.71	0.086	6.35	33.61
3	5.62	0.196	274.7	4.08	0.66	0.081	6.36	32.44
4	7.55	0.268	271.1	3.90	0.71	0.094	6.08	22.71
5	5.26	0.199	247.5	3.35	0.55	0.099	5.22	26.15
6	5.71	0.198	280.4	3.26	0.54	0.104	5.09	25.69
7	5.44	0.235	275.1	3.14	0.54	0.109	4.90	20.87
8	6.34	0.205	255.4	2.67	0.52	0.148	4.17	20.31
9	9.29	0.388	253.6	3.51	0.95	0.155	5.47	14.11
10	7.16	0.288	259.9	4.57	1.01	0.098	7.12	24.74
11	4.96	0.118	268.6	5.38	0.65	0.045	8.40	71.51
12	5.45	0.213	266.3	5.62	1.28	0.082	8.77	41.14
13	1.98	0.043	267.8	10.95	0.85	0.014	17.08	398.61
14	1.88	0.029	347.5	10.95	0.72	0.012	17.08	577.25
15	1.32	0.091	261.3	9.55	0.79	0.017	14.90	164.14
16	1.45	0.192	260.2	8.13	0.96	0.029	12.68	65.93

capillary spectral peak of Hwang and Fois (2015) emerging at around k = 370 rad/m u_* near the gravity-capillary minimum phase speed c_m = 0.23 m/s. Spectra produced from past observations are displayed in Figure 7. Those of Yurovskaya et al. (2013) and Laxague et al. (2015) exhibit the lowest amount of separation in range between low wind forcing and higher wind forcing. The laboratory measurements of Jähne and Riemer (1990) and the field measurements of Hara et al. (1998) show striking similarity to RaDyO spectra in their range of spectral densities, though each has a different tail shape for moderate to high wind forcing.

Figure 8 provides the peak wave numbers extracted from the saturation spectra shown in Figure 6. While some spectra show little variation of the peak wave number with respect to wind forcing (Hwang et al., 1996; Laxague et al., 2015), most others indicate a sharp transition from decimeter-scale wavelength to a centimeter-scale wavelength with increased forcing. For some of the models (Hwang & Fois, 2015; Yurovskaya et al., 2013), this is shown to occur at the point u_* is near to the gravity-capillary minimum phase speed c_m = 0.23 m/s. For the model of Elfouhaily et al. (1997), the observations of Jähne and Riemer (1990), and the RaDyO spectra, this transition begins at lower wind forcing—u_* ~0.12 m/s for the former and u_*~0.045 m/s for the latter two. The two departures from this paradigm within the RaDyO set are noted in Figure 8 and correspond to run numbers 12 and 16. These two cases have notably high long wave steepness as indicated in Table 1. Figure 8b shows the RaDyO results alongside the wave numbers of peak wave growth from the laboratory measurements and stability theory of Kawai (1979a, 1979b). Note the sharp transition which occurs at the critical friction velocity u_{*crit}~0.045 m/s and the ensuing near-asymptotic behavior trending toward k_m (corresponding to the gravity-capillary minimum phase speed c_m~0.23 m/s).

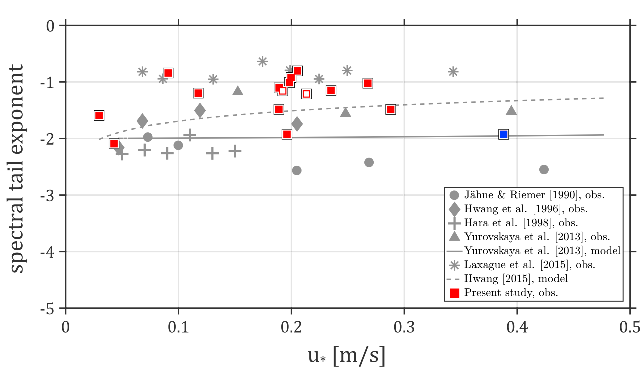

Figure 9. Slope of the omnidirectional saturation spectral high wave number tails in log-log space, shown alongside the selected observational and modeled results.

The slopes of the spectral tail in log-log space are given in Figure 9. In order to provide the appropriate comparison across all spectra, the tails were computed over the portion of the capillary regime sensed during RaDyO: 1,173 < k < 1,600 rad/m. No discernible sensitivity of this parameter to wind forcing is found among the RaDyO data. The same is true for the spectra produced from models and other observations, all shown alongside the RaDyO results. The model of Yurovskaya et al. (2013) parameterizes the presence of parasitic capillaries and therefore has a tail which is of shallower slope than that of its source material, Kudryavtsev et al. (1999). In general, the model spectra have steeper high wave number spectral tails than do the spectra computed from the RaDyO data.

Outliers in Figures 8 and 9 correspond to runs 12 and 16, two cases marked by low wind forcing and long gravity waves of moderate steepness. This wave-induced change in the gravity-capillary surface

10.1029/2018JC013859

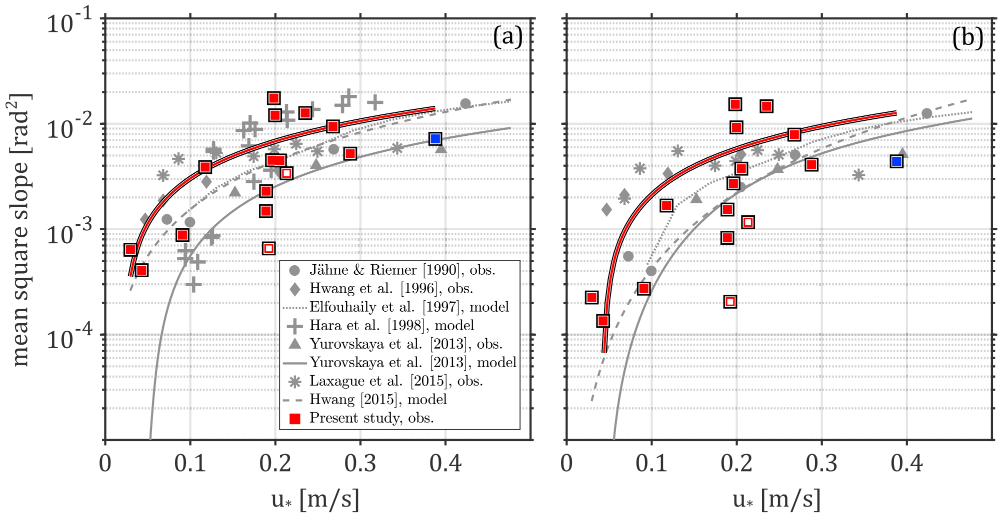

Figure 10. Mean square slope as a function of friction velocity, computed over (a) $112.7 < k < 371$ and (b) $371 < k < 1{,}173$, corresponding to GC1 and GC2, respectively. Hara et al. (1998) results exist only in a due to their spectra not being defined for $k > 800$ rad/m. The outliers and special case noted in Figure 8 are again represented as open squares and a blue square, respectively.

roughness is consistent with the laboratory observations of Laxague, Curcic, et al. (2017). Given the reduction of mean square slope and the shifting of the gravity-capillary spectral peak to lower wave numbers, gravity wave modulation of airflow is likely the dominant process affecting these changes; this wave-wind interaction has been noted in recent laboratory (Buckley & Veron, 2016) and field observations (Grare, Lenain, et al., 2013).

The wave number position of the saturation spectral peak is directly tied to the share of mean square slope contained within each short wave subrange. Figure 10 displays mean square slope computed over GC1 (a) and GC2 (b) as functions of u_*. Within GC1, there is a consistency between Jähne and Riemer (1990), Hwang et al. (1996), Elfouhaily et al. (1997), Hwang and Fois (2015), and the curve of best fit to the RaDyO data, with roughness computed from the spectra of Hara et al. (1998) showing an even sharper increase with wind forcing. For GC2, the model spectra of Yurovskaya et al. (2013) join this group in general agreement, while Hwang et al. (1996) depart it. Over both subranges, the partitioned slope variance computed from the observational spectra of Yurovskaya et al. (2013) agrees quite well with those obtained during RaDyO. The dramatic increase in RaDyO GC-scale roughness occurs for friction velocity magnitudes greater than u_{*crit}~0.045 m/s, the forcing regime in which the gravity-capillary spectral peak emerges. Surface wave slope variance computed from the observational spectra of Laxague et al. (2015) show a conspicuous insensitivity to wind forcing shown. Similar behavior was noted in Figure 7d, as the energy densities of the spectra themselves do not change much with wind forcing. Given this general wind insensitivity across all wave scales, it is likely that the sea surface slope fields computed for that study were compressed in their dynamic range.

A single case study representing a segment of high wind forcing and moderate wave height (peak wind sea height of ~0.5 m) is shown between Figures 11 and 13. For this case (#9 from Table 1), the wind and mean wave direction were nearly aligned in an east-northeast orientation ("going-toward" convention). For all three figures, a 10-s snippet is taken from the overall time series in order to focus on the relationship between short gravity waves and gravity-capillary waves. A signal with period 1–2 s is seen clearly in the gravity-capillary wave subrange of the spectrogram in Figure 11. This signal is collapsed into one dimension by computing the aforementioned quantities k_p and mean square slope over the gravity-capillary regimes (GC1 and GC2). The water surface elevation and slope time series are shown in Figure 12, represented as violet and teal lines, respectively. The slope has a dominant period of ~1.7 s, approximately twice that of the elevation. Movies S2–S4 are intended to serve as accompaniments to this segment of the data. They are composed of the integrated elevation field alongside the directional wave number spectrum (S2) and 2-D PDF time series (S3) and an animation of the slope field component time series (S4).

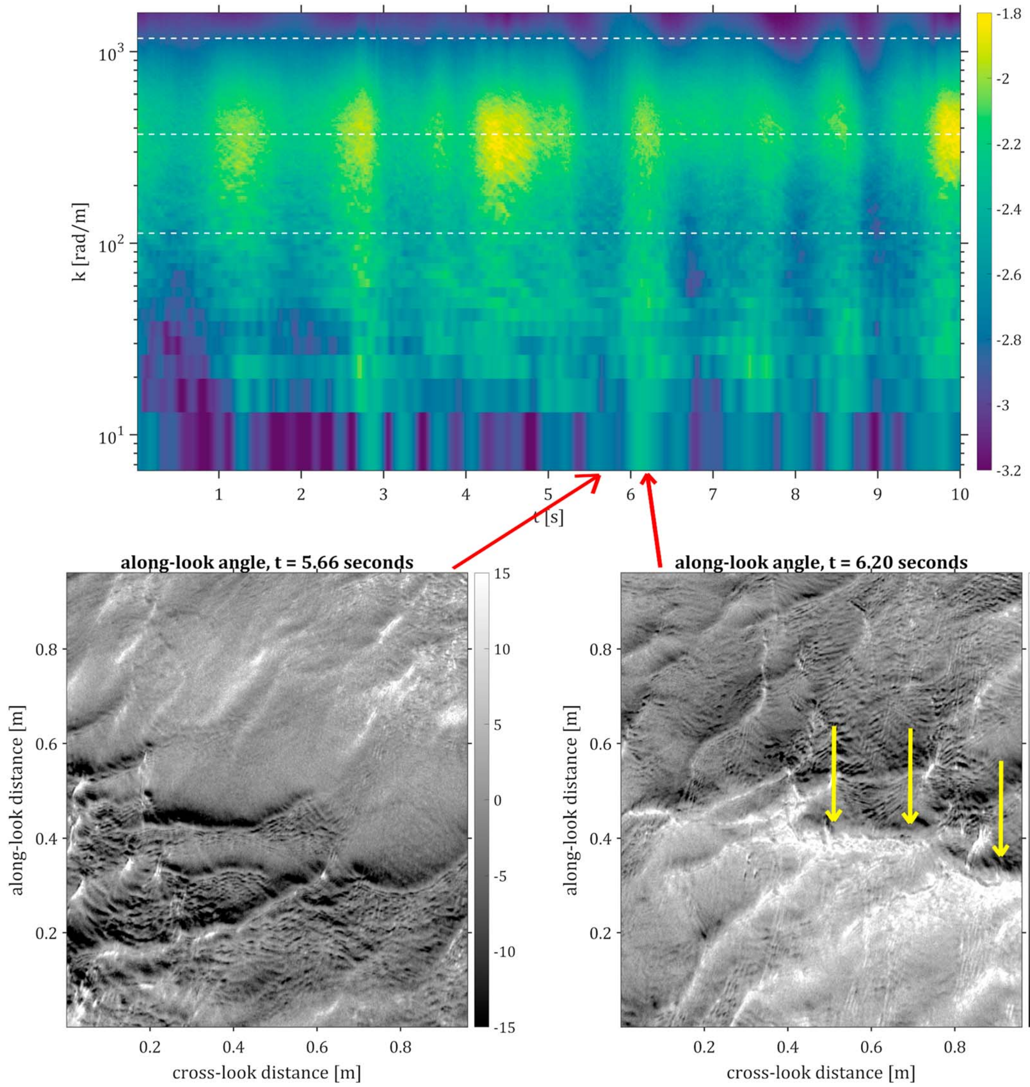

Figure 11. Case study: Run 9. Wave number saturation spectrogram, 10-s segment. The color indicates omnidirectional saturation spectral density (dimensionless). The horizontal dashed lines mark k = 112.7, 371, and 1,173 rad/m, respectively. The red arrows mark the times from which the example slope fields are taken, with color bars on those subfigures indicating angle in degrees. Note the crest of the microbreaker (indicated by yellow arrows) in the center of the slope field at t = 6.20 s.

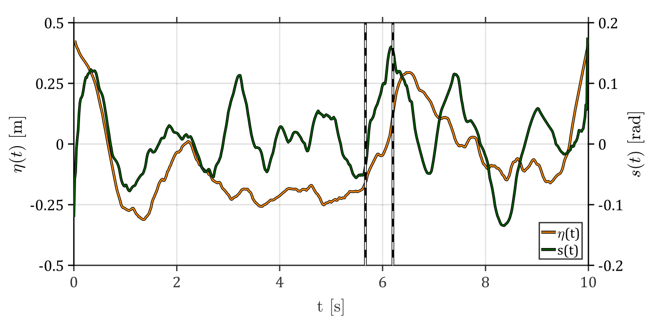

Figure 12. Case study: Run 9. Time series of water surface elevation η (t) (as measured by the lidar) and local water surface slope s (t) (as computed from a 1-cm diameter virtual wave slope gauge in the center of the polarimetric slope fields), shown as dashed green and solid orange lines, respectively. Times of smooth/microbreaking examples from Figure 11 are marked in vertical black and white dashed white lines.

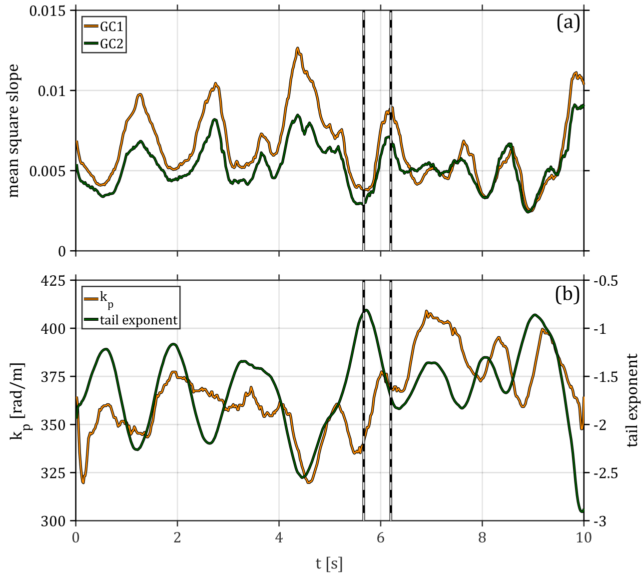

Figure 13. Case study: Run 9. (a) Time series of mean square slope in the gravity-capillary subrange #1 (orange solid) and mean square slope in the gravity-capillary subrange #2 (green dashed). (b) Time series of peak wave number (orange solid) and the high wave number spectral tail exponent (green dashed). All parameters are computed from spectra produced using the entire slope fields. Times of smooth/microbreaking examples from Figure 11 are indicated by vertical black and white dashed lines.

4. Discussion

The slope field observations obtained during RaDyO allowed for the determination of directional short wave spectra. These were used in tandem with the observed wind stress and gravity wave data set to describe the response of gravity-capillary waves to the air-sea momentum flux. The analysis of this study focused on one, a comparative analysis of time-averaged short wave spectral features and atmospheric forcing, and two, an event study centered on the modulation of short wave properties due to microbreaking in a young wind sea.

For the first component of the analysis, omnidirectional wave number spectra formed the foundation of the analysis. As seen in Figures 6 and 7, no single model or set of other observations match the RaDyO results at all wave numbers. These spectra are characterized by a broad range of energy density in the gravity-capillary subrange as a function of wind forcing, the clear emergence of a gravity-capillary peak near k_m and a general slope constancy in the highest wave number (pure capillary) subrange. The model of Yurovskaya et al. (2013) provides spectra which show separation with wind forcing that is qualitatively close to the RaDyO observations. The model of Hwang and Fois (2015) also captures this separation in addition to agreeing with these observations in gravity-capillary spectral peak and capillary tail shape. Over the short gravity wave subrange ($k < 1$,12.7 rad/m), RaDyO spectra show much higher variance in spectral density than those produced from models (Figures 6b–6d) or observations (Figure 7). Because of the strict rejection criteria and careful image selection regarding Sun glint, we do not believe that this variance is the result of image saturation. This is evident in the shape of the spectra themselves, as Sun glint-related contamination affects all scales of waves, especially obscuring the centimeter-scale features which are so well-resolved in the present data set. A potential source of this variance is the poor resolution of longer waves due to the imager's small frame size: Each slope field contains relatively few gravity waves from which spatial information can be recovered.

For low wind forcing, the saturation spectral peak lies at k of order 10 rad/m, in the decimeter-scale waves which are predominantly restored to equilibrium by gravity (Figure 8). The transition of the spectral peak toward the gravity-capillary subrange occurs near u_*~0.045 m/s, the "critical wind friction velocity" according to classic air side stability analysis (Kawai, 1979b) and laboratory measurements (Kawai, 1979a). Furthermore, the wave number peaks of the RaDyO saturation spectra align closely with the wave numbers at which peak wave growth occurs in the Kawai (1979a, 1979b) results, as shown in Figure 8b. This consistency between theoretical, laboratory, and field results highlights the saturation spectral peak as the most rapidly growing scale. It follows directly that the degree to which wave models are able to describe the crucial physical process of short wave growth at low wind forcing is dependent upon their ability to capture this observed transition in spectral shape. None of the models referenced in this study (Elfouhaily et al., 1997; Hwang & Fois, 2015; Yurovskaya et al., 2013) show this transition in gravity-capillary subrange shape beginning at the Kawai (1979a, 1979b) critical wind forcing level.

The RaDyO results show a dramatic increase in surface slope variance among gravity-capillary waves (Figure 10). Similar characteristics are also seen in reanalysis of classic laboratory measurements (Jähne & Riemer, 1990) and in model spectra that were specifically designed with radar remote sensing in mind (Elfouhaily et al., 1997; Hwang & Fois, 2015). The wind sensitivity of gravity-capillary surface roughness as inferred from RaDyO spectra is quite close to that produced from the hybrid stereoscopic system of Kosnik & Dulov (2011) as described in Yurovskaya et al. (2013). In the GC2 subrange, both of these stand in stark contrast to the weaker wind sensitivity of the Hwang et al. (1996) and Laxague et al. (2015) surface slope variances. For the latter study (Laxague et al., 2015), it does not appear that the ocean surface response to wind forcing of different magnitudes has been captured appropriately. The greatest contributor to this shortcoming is the blurring of gravity-capillary waves which propagate during the ~10-ms camera exposure time used for that study (an order of magnitude longer than the exposure time used here). Short waves which are "bound" to (that is, advected by) the dominant longer waves will propagate much faster than their intrinsic celerity (Plant, Keller, et al., 1999), exacerbating the problem. This results in unwanted smoothing over the gravity-capillary scales, therefore reducing observed slope amplitudes as positive and negative slopes are averaged to near-zero values. At the smallest scales, this becomes extreme: For a nominal bound wave celerity of 1 m/s, scales smaller than 1 cm will be completely obscured over the 10-ms exposure time. An additional result of this blurring is the reduced sensitivity of the device to roughness produced from increased wind forcing, compressing the dynamic range of the spectral energy densities as seen in Figure 7d.

The second component of the analysis is an investigation of the study's highest observed wind forcing and the identification of a microbreaking event. Microbreaking is the breaking of short-scale gravity-capillary waves which occurs without the entrainment of air (Banner & Phillips, 1974). It is theorized to play a crucial role in the growth of wind waves (Kudryavtsev & Chapron, 2016). Structurally, microbreakers have turbulent bore-like crests with dimpled surface roughness features at and upwind of the crests (Zappa et al., 2001, 2004). The parasitic capillaries immediately downwind of the bore-like crest are observed to diminish. In the wake of the microbreaker, the turbulence suppresses the growth of capillary waves. Also, the bore-like crest and its turbulent wake disturb the ocean skin layer, making microbreakers detectable through thermal infrared imaging (Zappa et al., 2001, 2004). Note that not all gravity-capillary waves are microbreakers.

As seen in Figures 11–13, short wave spectral parameters are modulated as a result of interaction between strong wind forcing and gravity-subrange wind sea (C_p/u_* ~14.11). The dominant period of the wave slope time series was 1.7 s, approximately half of the wind sea peak period of 3.51 s. Based on the example time series shown in Figures 12 and 13 (and the Supporting Information videos), we see that this is the result of enhanced microbreaking at the crest of the dominant wind sea, a result of the straining of short wave packets by the long wave orbital motions (Phillips & Banner, 1974). For comparison, note the structure of these short wave slope fields alongside mean square slope, k_p, and the high wave number tail slope at the dashed lines in Figures 12 and 13: Microbreakers are seen forward of the crest of a traversing steep dominant wave (T~3 s). After the microbreakers pass, gravity-capillary scale surface roughness is reduced and the saturation spectral peak shifts to higher wave numbers as the air-sea interface becomes smoother (as observed in the Supporting Information video).

This steepening, breaking, and resteepening can effectively halve the period of oscillation of the observed slope signal. Such a phenomenon may occur if the breaking is strong enough to alter the local wave slope (and therefore be sensed via the polarimeter) yet is too weak to appreciably reduce the wave amplitude (and therefore evade detection by the lidar). By comparing the water surface elevation frequency spectrum computed from the lidar time series and the water surface elevation frequency spectrum converted from the polarimetric slope wave number spectrum (Figure S1), we estimate the RMS water surface elevation of the camera-resolved waves (wavelengths between 1 mm and 1 m) to be less than 1% of the value estimated from the dominant wind waves resolved by the lidar (wavelengths greater than 10 cm). Despite this disparity, even low-amplitude short waves vary substantially in wave slope, maximizing at ~0.15 rad, which is nearly identical to the long wave steepness of Run 9 shown in Table 1. At the moment of breaking, the point slope is at a local temporal maximum (the second dashed line in Figure 12). Mean square slopes computed over both GC1 and GC2 are also at local maxima, and the high wave number spectral tail is at its steepest (Figure 13). The modulation of the short wave characteristics is substantial: Over the duration of Run 9, mean square slope, k_p, and the spectral tail exponent vary from the mean over the wind sea period by 50%, 20%, and 50%, respectively.

5. Conclusions

We have made new observations of short-scale ocean surface waves during low and moderate wind forcing conditions, highlighting key aspects of the complexity of the behavior of the gravity-capillary scales of the sea surface roughness. Spectral analysis was used to distill these dense data sets into simpler, more easily understood parameters. The saturation spectral peaks are found near k_m = 371 rad/m. Both the RaDyO results and observations and the RaDyO results reveal that the level of wind forcing at which this peak emerges is lower than classic models indicate (Elfouhaily et al., 1997; Hwang & Fois, 2015; Yurovskaya et al., 2013). This transition is observed to begin near the critical friction velocity for short wave growth (u_*~0.045 m/s; Kawai, 1979a, 1979b), strongly implying that such an emergence is due to wave growth that results from a transition in air side flow stability (Kawai, 1979a, 1979b). However, further measurements are required to pin down the exact wind forcing magnitude at which this occurs, as laboratory measurements have placed it above (Donelan & Plant, 2009) and below (Kahma & Donelan, 1988) u_{*crit}~0.045 m/s. In any case, even the low-forcing observational data of RaDyO are too strongly forced to evaluate this discrepancy. Finally, for higher magnitudes of wind forcing and in the presence of steep gravity waves, microbreaking events are shown to strongly impact short wave spectral characteristics and centimeter-scale surface roughness. Further study is warranted in light of the findings of the recent simulation study of Sullivan et al. (2018), which found significant consequences for air-sea interaction energy and scalar fluxes associated with the variability of strongly-forced sea surface roughness elements, which is particularly relevant to the gravity-capillary wave scales.

The sea surface waves which are restored to equilibrium by both gravity and capillarity occupy a special place within air-sea interaction. They are strongly impacted by interactions with larger-scale gravity waves and yet do not have the scale to appreciably contribute to the overall wave energy. However, they are hypothesized to be the principal mediators of air-sea momentum flux (Donelan & Plant, 2009; Kudryavtsev & Makin, 2002) and can significantly contribute to air-sea gas exchange as microscale breakers (Zappa et al., 2001, 2004). The present work was designed with the intention of describing this class of ocean surface waves in the context of physical forcing and microscale breaking through novel field observations and intensive analysis. We anticipate that the results presented here will provide a useful basis for characterizing the gravity-capillary subrange of ocean surface wave spectra.

Appendix A: Smoothing Filters

Smoothing filters were not applied to the wave slope fields obtained during RaDyO. This is primarily due to the effect that they have on the spectra and associated integral moments. As shown in Figure A1, wave spectral shape is profoundly changed by both median filters (Huang et al., 1979; here executed as MATLAB's "medfilt2.m" function) and spatial convolution filters (Roberts & Roberts, 1978), shifting the wave number

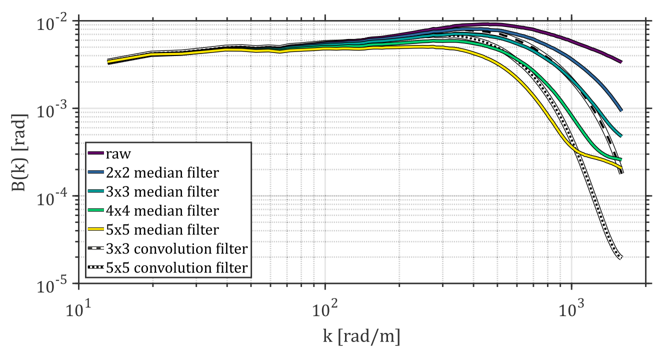

Figure A1. Example omnidirectional saturation spectra generated from slope fields subjected to the smoothing functions listed in the figure legend.

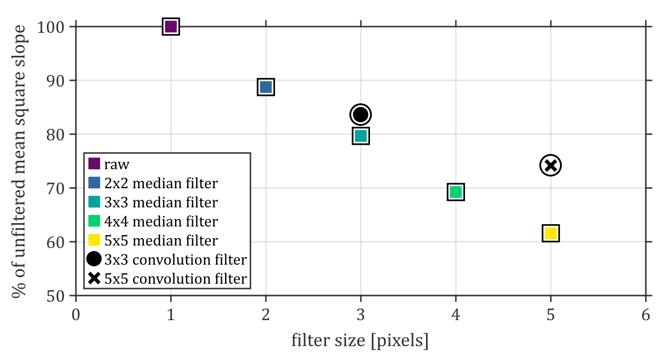

Figure A2. Mean square slope computed from the spectra shown in Figure A1 ($\int k^{-1}B(k)dk$) with the same smoothing functions. Represented as a percentage of the mean square slope of the unfiltered wave slope fields.

position of the spectral peak and drastically increasing the tail slope magnitude. Furthermore, mean square slope computed over the full wave number range has a substantial dependence upon the filter type and size (Figure A2). In the absence of a secondary, external "ground truth" on FLIP to serve as a reference measurement for surface roughness, we did not feel comfortable with choosing one filter type over another and decided to abstain from applying one altogether. The slope fields of Jähne and Riemer (1990) were subjected to 3 × 3 median filters before their Fourier transforms were applied; this may account for the difference in spectral tail slope between those spectra and the ones obtained from the slope fields collected during RaDyO.

Acknowledgments

The authors have no conflicts of interest to declare. This work was funded by the Office of Naval Research under the Radiance in a Dynamic Ocean (RaDyO) DRI, with grants N00014-06-1-0372 and N00014-11-1-0168 (C. Zappa) and N00014-06-1-0047 and N00014-11-1-0054 (M. Banner). The authors are grateful to the scientists, technicians, and crewmembers who were involved in the RaDyO project. Thanks are given to Maria Yurovskaya, Vladimir Kudryavtsev, and Paul Hwang for providing the codes used to produce their model wave number spectra. The data used for this work have been archived for public access with the Columbia University Academic Commons (https://doi.org/10.7916/D8HQ56ZV). This is Lamont-Doherty Earth Observatory contribution 8218.

References

Banner, M. L., & Phillips, O. M. (1974). On the incipient breaking of small scale waves. *Journal of Fluid Mechanics*, *65*(04), 647. https://doi.org/10.1017/S0022112074001583

Benetazzo, A. (2006). Measurements of short water waves using stereo matched image sequences. *Coastal Engineering*, *53*(12), 1013–1032. https://doi.org/10.1016/j.coastaleng.2006.06.012

Buckley, M. P., & Veron, F. (2016). Structure of the airflow above surface waves. *Journal of Physical Oceanography*, *46*(5), 1377–1397. https://doi.org/10.1175/JPO-D-15-0135.1

Caulliez, G., & Guérin, C.-A. (2012). Higher-order statistical analysis of short wind wave fields. *Journal of Geophysical Research*, *117*, C06002. https://doi.org/10.1029/2011JC007854

Cox, C., & Munk, W. (1954). Measurement of the roughness of the sea surface from photographs of the Sun's glitter. *Journal of the Optical Society of America*, *44*(11), 838–850. https://doi.org/10.1364/JOSA.44.000838

Divins, D. L., & Metzger, D. (2017). NGDC coastal relief model. Retrieved November 1, 2017, from http://sccoos.org/data/bathy

Donelan, M. A., & Plant, W. J. (2009). A threshold for wind-wave growth. *Journal of Geophysical Research*, *114*, C07012. https://doi.org/10.1029/2008JC005238

Kosnik, M. V., & Dulov, V. A. (2011). Extraction of short wind wave spectra from stereo images of the sea surface. *Measurement Science and Technology*, *22*(1), 15504. https://doi.org/10.1088/0957-0233/22/1/015504

Edson, J. B., Jampana, V., Weller, R. a., Bigorre, S. P., Plueddemann, A. J., Fairall, C. W., et al. (2013). On the exchange of momentum over the open ocean. *Journal of Physical Oceanography*, *43*(8), 1589–1610. https://doi.org/10.1175/JPO-D-12-0173.1

Elfouhaily, T., Chapron, B., Katsaros, K., & Vandemark, D. (1997). A unified directional spectrum for long and short wind-driven waves. *Journal of Geophysical Research*, *102*, 15,781–15,796. https://doi.org/10.1029/97JC00467

Frew, N. M., Bock, E. J., Schimpf, U., Hara, T., Haußecker, H., Edson, J. B., et al. (2004). Air-sea gas transfer: Its dependence on wind stress, small-scale roughness, and surface films. *Journal of Geophysical Research*, *109*, C08S17. https://doi.org/10.1029/2003JC002131

Grare, L., Lenain, L., Melville, W. K., Grare, L., Lenain, L., & Melville, W. K. (2013). Wave-coherent airflow and critical layers over ocean waves. *Journal of Physical Oceanography*, *43*(10), 2156–2172. https://doi.org/10.1175/JPO-D-13-056.1

Grare, L., Peirson, W. L., Branger, H., Walker, J. W., Giovanangeli, J.-P., & Makin, V. K. (2013). Growth and dissipation of wind-forced, deep-water waves. *Journal of Fluid Mechanics*, *722*, 5–50. https://doi.org/10.1017/jfm.2013.88

Hara, T., Bock, E. J., Edson, J. B., & McGillis, W. R. (1998). Observation of short wind waves in coastal waters. *Journal of Physical Oceanography*, *28*(7), 1425–1438. https://doi.org/10.1175/1520-0485(1998)028<1425:Ooswwi>2.0.co;2

Harker, M., & O'Leary, P. (2008). Least squares surface reconstruction from measured gradient fields. In 2008 IEEE Conference on Computer Vision and Pattern Recognition (pp. 1–7). IEEE. doi:https://doi.org/10.1109/CVPR.2008.4587414

Harris, F. J. (1978). On the use of windows for harmonic analysis with the discrete Fourier transform. *Proceedings of the IEEE*, *66*(1), 51–83. https://doi.org/10.1109/PROC.1978.10837

Huang, T., Yang, G., & Tang, G. (1979). A fast two-dimensional median filtering algorithm. *IEEE Transactions on Acoustics, Speech, and Signal Processing*, *27*(1), 13–18. https://doi.org/10.1109/TASSP.1979.1163188

Hwang, P. A., Atakturk, S., Sletten, A., Trizna, D. B., & Rizna, D. E. B. T. (1996). A study of the wavenumber spectra of short water waves in the ocean. *Journal of Physical Oceanography*, 1266–1285. https://doi.org/10.1175/1520-0485(1996)026<1266:ASOTWS>2.0.CO%3B2

Hwang, P. A., & Fois, F. (2015). Surface roughness and breaking wave properties retrieved from polarimetric microwave radar backscattering. *Journal of Geophysical Research: Oceans*, *120*, 3640–3657. https://doi.org/10.1002/2015JC010782

Jähne, B., & Riemer, K. (1990). Two-dimensional wave number spectra of small-scale water surface waves. *Journal of Geophysical Research*, *95*, 11–531. https://doi.org/10.1029/JC095iC07p11531

Jin, Z., Charlock, T. P., Rutledge, K., Stamnes, K., & Wang, Y. (2006). Analytical solution of radiative transfer in the coupled atmosphere-ocean system with a rough surface. *Applied Optics*, *45*(28), 7443–7455. https://doi.org/10.1364/AO.45.007443

Kahma, K. K., & Donelan, M. A. (1988). A laboratory study of the minimum wind speed for wind wave generation. *Journal of Fluid Mechanics*, *192*(1), 339–364. https://doi.org/10.1017/S0022112088001892

Kawai, S. (1979a). Discussion on the critical wind speed for wind-wave generation on the basis of shear-flow instability theory. *Journal of the Oceanographical Society of Japan*, *35*(5), 179–186. https://doi.org/10.1007/BF02108637

Kawai, S. (1979b). Generation of initial wavelets by instability of a coupled shear flow and their evolution to wind waves. *Journal of Fluid Mechanics*, *93*(04), 661. https://doi.org/10.1017/S002211207900197X

Kudryavtsev, V., & Chapron, B. (2016). On growth rate of wind waves: Impact of short-scale breaking modulations. *Journal of Physical Oceanography*, *46*(1), 349–360. https://doi.org/10.1175/JPO-D-14-0216.1

Kudryavtsev, V., & Makin, V. K. (2002). Coupled dynamics of short waves and the airflow over long surface waves. *Journal of Geophysical Research*, *107*(C12), 3209. https://doi.org/10.1029/2001JC001251

Kudryavtsev, V., Makin, V. K., & Chapron, B. (1999). Coupled sea surface-atmosphere model: 2. Spectrum of short wind waves. *Journal of Geophysical Research*, *104*, 7625–7639. https://doi.org/10.1029/1999JC900005

Laxague, N. J. M. (2016). Development and application of gravity-capillary wave Fourier analysis for the study of air-sea interaction physics. Open Access Dissertations. Retrieved from http://scholarlyrepository. Miami.Edu/oa_dissertations/1771

Laxague, N. J. M., Curcic, M., Björkqvist, J.-V., & Haus, B. K. (2017). Gravity-capillary wave spectral modulation by gravity waves. *IEEE Transactions on Geoscience and Remote Sensing*, *55*(5), 1–9. https://doi.org/10.1109/TGRS.2016.2645539

Laxague, N. J. M., Haus, B. K., Bogucki, D., & Özgökmen, T. (2015). Spectral characterization of fine-scale wind waves using shipboard optical polarimetry. *Journal of Geophysical Research*, *120*, 3140–3156. https://doi.org/10.1002/2014JC010403
Laxague, N. J. M., Haus, B. K., Ortiz-Suslow, D. G., Smith, C. J., Novelli, G., Dai, H., et al. (2017). Passive optical sensing of the near-surface wind-driven current profile. *Journal of Atmospheric and Oceanic Technology*, *34*(5), 1097–1111. https://doi.org/10.1175/JTECH-D-16-0090.1
Lenain, L., & Melville, W. K. (2017). Measurements of the directional spectrum across the equilibrium-saturation ranges of wind-generated surface waves. *Journal of Physical Oceanography*. https://doi.org/10.1175/JPO-D-17-0017.1
Maxwell, J. C. (1890). Capillary action. The Scientific Papers of James Clerk Maxwell.
Mironov, A. S., Yurovskaya, M. V., Dulov, V. A., Hauser, D., & Guérin, C. A. (2012). Statistical characterization of short wind waves from stereo images of the sea surface. *Journal of Geophysical Research*, *117*, C007860. https://doi.org/10.1029/2011JC007860
Munk, W. (2009). An inconvenient sea truth: Spread, steepness, and skewness of surface slopes. *Annual Review of Marine Science*, *1*(1), 377–415. https://doi.org/10.1146/annurev.marine.010908.163940
Phillips, O. M. (1984). On the response of short ocean wave components at a fixed wavenumber to ocean current variations. *Journal of Physical Oceanography*. https://doi.org/10.1175/1520-0485(1984)014<1425:OTROSO>2.0.CO;2
Phillips, O. M., & Banner, M. L. (1974). Wave breaking in the presence of wind drift and swell. *Journal of Fluid Mechanics*, *66*(04), 625. https://doi.org/10.1017/S0022112074000413
Plant, W. J. (2002). A stochastic, multiscale model of microwave backscatter from the ocean. *Journal of Geophysical Research*, *107*(C9), 3120. https://doi.org/10.1029/2001JC000909
Plant, W. J. (2009). The ocean wave height variance spectrum: Wavenumber peak versus frequency peak. *Journal of Physical Oceanography*, *39*(9), 2382–2383. https://doi.org/10.1175/2009JPO4268.1
Plant, W. J., Dahl, P. H., & Keller, W. C. (1999). Microwave and acoustic scattering from parasitic capillary waves. *Journal of Geophysical Research*, *104*, 25,853–25,866. https://doi.org/10.1029/1999JC900168
Plant, W. J., Keller, W. C., Hesany, V., Kara, T., Bock, E., & Donelan, M. A. (1999). Bound waves and Bragg scattering in a wind-wave tank. *Journal of Geophysical Research*, *104*, 3243–3263. https://doi.org/10.1029/1998JC900061
Roberts, J., & Roberts, T. D. (1978). Use of the Butterworth low-pass filter for oceanographic data. *Journal of Geophysical Research*, *83*, 5510–5514. https://doi.org/10.1029/JC083iC11p05510
Sullivan, P. P., Banner, M. L., Morison, R. P., & Peirson, W. L. (2018). Turbulent flow over steep steady and unsteady waves under strong wind forcing. *Journal of Physical Oceanography*, *48*(1), 3–27. https://doi.org/10.1175/JPO-D-17-0118.1
Wei, J., Lewis, M. R., Van Dommelen, R., Zappa, C. J., & Twardowski, M. S. (2014). Wave-induced light field fluctuations in measured irradiance depth profiles: A wavelet analysis. *Journal of Geophysical Research: Oceans*, *119*, 1344–1364. https://doi.org/10.1002/2013JC009572
Wu, J. (1982). Wind-stress coefficients over sea surface from breeze to hurricane. *Journal of Geophysical Research*, *87*, 9704–9706. https://doi.org/10.1029/JC087iC12p09704
You, Y., Kattawar, G. W., Voss, K. J., Bhandari, P., Wei, J., Lewis, M., et al. (2011). Polarized light field under dynamic ocean surfaces: Numerical modeling compared with measurements. *Journal of Geophysical Research*, *116*, C00H05. https://doi.org/10.1029/2011JC007278
Yurovskaya, M. V., Dulov, V. A., Chapron, B., & Kudryavtsev, V. N. (2013). Directional short wind wave spectra derived from the sea surface photography. *Journal of Geophysical Research: Oceans*, *118*, 4380–4394. https://doi.org/10.1002/jgrc.20296
Zappa, C. J., Asher, W. E., & Jessup, A. T. (2001). Microscale wave breaking and air-water gas transfer. *Journal of Geophysical Research*, *106*, 9385–9391. https://doi.org/10.1029/2000JC000262
Zappa, C. J., Asher, W. E., Jessup, A. T., Klinke, J., & Long, S. R. (2004). Microbreaking and the enhancement of air-water transfer velocity. *Journal of Geophysical Research*, *109*, C08S16. https://doi.org/10.1029/2003JC001897
Zappa, C. J., Banner, M. L., Schultz, H., Corrada-Emmanuel, A., Wolff, L. B., & Yalcin, J. (2008). Retrieval of short ocean wave slope using polarimetric imaging. *Measurement Science and Technology*, *19*(5), 055503. https://doi.org/10.1088/0957-0233/19/5/055503
Zappa, C. J., Banner, M. L., Schultz, H., Gemmrich, J. R., Morison, R. P., Lebel, D. A., & Dickey, T. (2012). An overview of sea state conditions and air-sea fluxes during RaDyO. *Journal of Geophysical Research*, *117*, C00H19. https://doi.org/10.1029/2011JC007336

Erratum

In the originally published version of this article, there was an error in first paragraph of section 2. The text originally read “six axis inertial motion unit” which was incorrect. This has been changed to “six degree of freedom inertial motion unit”. This version may be considered the authoritative version of record.